The Thermally Driven Cross-Basin Circulation in Idealized Basins under Varying Wind Conditions

MANUELA LEHNER AND C. DAVID WHITEMAN

University of Utah, Salt Lake City, Utah

(Manuscript received 2 September 2011, in final form 10 January 2012)

ABSTRACT

The Weather Research and Forecasting model is used to perform large-eddy simulations of thermally driven cross-basin winds in idealized, closed basins. A spatially and temporally varying heat flux is prescribed at the surface as a function of slope inclination and orientation to produce a horizontal temperature gradient across the basin. The thermal asymmetry leads to the formation of a closed circulation cell flowing toward the more strongly heated sidewall, with a return flow in the upper part of the basin. In the presence of background winds above the basin, a second circulation cell forms in the upper part of the basin, resulting in one basin-sized cell, two counterrotating cells, or two cells with perpendicular rotation axes, depending on the background-wind direction with respect to the temperature gradient. The thermal cell near the basin floor and the background-wind-induced cell interact with each other either to enhance or to reduce the thermal cross-basin flow and return flow. It is shown that in 5–10-km-wide basins cross-basin temperature differences that are representative of east- and west-facing slopes are insufficient to maintain perceptible cross-basin winds because of reduced horizontal temperature and pressure gradients, particularly in a neutrally stratified atmosphere.

1. Introduction

Solar irradiation in mountainous terrain is strongly inhomogeneous, depending on the inclination and the orientation of the surface with respect to the sun (Whiteman et al. 1989; Matzinger et al. 2003; Hoch and Whiteman 2010). Spatial temperature variations resulting from irradiation inhomogeneities may produce local pressure variations and thus affect the wind circulation. Valley and basin topographies with two opposing mountain sidewalls generally lead to asymmetric irradiation with respect to the valley axis or basin center, thus favoring the occurrence of cross-valley or cross-basin flows from the less strongly sunlit to the more strongly sunlit sidewall. The term cross-valley circulation has been used in some studies to describe the two-dimensional circulation induced by slope winds (e.g., Kuwagata and Kimura 1997; Rampanelli et al. 2004). In this study, however, we define cross-valley flow or cross-basin flow (CBF) only as a flow across the valley or basin from one sidewall to the other, and we define cross-basin circulation as the circulation cell consisting of the CBF and a return flow (RF) aloft. Thermally driven cross-valley or cross-basin winds have been observed in the Columbia River valley, Canada (Gleeson 1951); in the Kananaskis Valley, Canada (MacHattie 1968); in the Dischma Valley, Switzerland (Hennemuth and Schmidt 1985; Hennemuth 1986; Urfer-Henneberger 1970); and in Arizona's Meteor Crater (Lehner et al. 2011).

This paper is a continuation of research reported by Lehner et al. (2011), in which data from the Meteor Crater Experiment (METCRAX) field campaign in Arizona's Meteor Crater (Whiteman et al. 2008) were analyzed to observe the diurnal cycle of cross-basin winds in the crater. Mean surface cross-basin winds in the Meteor Crater were on the order of 0.5–1 m s^{-1} on the approximately 500-m-wide crater floor. Under quiescent conditions above the crater surface, winds in the center of the crater were shown to be strongly related to the difference in global radiation, temperature, and pressure between two opposite crater sidewalls. Observations of the CBF were mostly confined to the surface, however, and the authors also found that under conditions with strong background winds above the crater rim a thermal CBF was not generally present at the crater floor.

In this study we use the Weather Research and Forecasting model (WRF) to systematically simulate the

Corresponding author address: Manuela Lehner, Dept. of Atmospheric Sciences, University of Utah, 135 S 1460 E, Rm. 819, Salt Lake City, UT 84112-0110.
E-mail: manuela.lehner@utah.edu

DOI: 10.1175/JAMC-D-11-0181.1

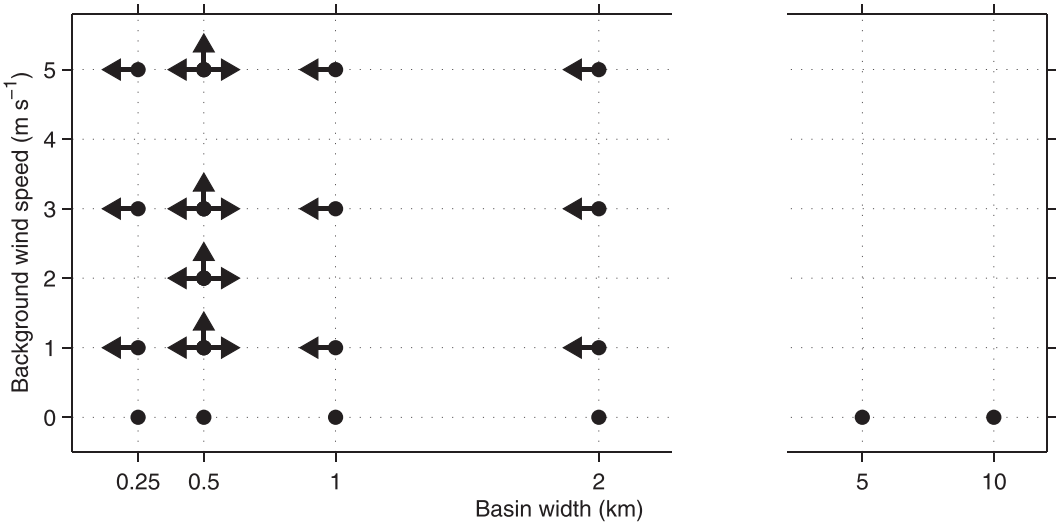

FIG. 1. Overview of all simulations and the respective combinations of background-wind speed, background-wind direction, and basin width. Arrows indicate the background-wind direction: up arrows denote southerly, left arrows denote easterly, and right arrows denote westerly background winds.

three-dimensional structure of the morning cross-basin circulation inside an idealized basin that is based on the topography of the Meteor Crater and to investigate the impact of background winds above the basin on the cross-basin circulation. A similar phenomenon is also known on a smaller spatial scale: namely, in street canyons. The formation of vortices by background winds or the channeling of background winds in street canyons in combination with temperature inhomogeneities across the street canyon has been investigated both observationally (Nakamura and Oke 1988; Offerle et al. 2007; Niachou et al. 2008) and numerically (Sini et al. 1996; Xie et al. 2005). To the authors' knowledge, however, thermally driven cross-basin or cross-valley flows and their interaction with winds above the basin or valley have not been studied yet on the larger scale of mountainous terrain.

This study focuses mainly on three parameters and their impact on the cross-basin circulation: 1) the background-wind speed, 2) the direction of the background wind with respect to the horizontal temperature gradient caused by asymmetric irradiation on the basin sidewalls, and 3) the width of the basin to determine the expected strength or the probability of occurrence of CBF in basins or valleys of different sizes. Figure 1 summarizes the respective combinations of wind speed, wind direction, and basin width for all 27 simulations. Simulations with a constant basin-floor width of 500 m (comparable to the Meteor Crater), varying background-wind speeds of 0–5 m s^{-1} and wind directions parallel, perpendicular, and opposite to the temperature gradient are described in section 3. Simulations with basins of different sizes, ranging from 250-m-wide to 10-km-wide basin floors, are discussed in section 4. The influence of atmospheric stability on the cross-basin circulation is not investigated systematically in this study. The diurnal change in stability caused by surface heating is used to evaluate the different response of the cross-basin circulation to the background wind under stable and neutral conditions, however. A sensible heat flux is prescribed at the surface that is representative in magnitude of the thermal forcing during the morning period at the Meteor Crater in October. The combination of the temporal evolution of the surface heat flux and a stably stratified initial sounding makes the idealized model results comparable to the development of the cross-basin circulation in the Meteor Crater between sunrise and noon. A comparison of model results and Meteor Crater observations is shown in section 2e.

2. Model setup

The simulations are performed with the Advanced Research WRF, version 3 (Skamarock et al. 2008), in large-eddy simulation (LES) mode. The LES capabilities of WRF have been tested and used in previous studies both over flat terrain (Antonelli and Rotunno 2007; Moeng et al. 2007) and over complex terrain (Catalano and Cenedese 2010; Catalano and Moeng 2010).

a. Model domain

The idealized basin topography is based on the topography of Arizona's Meteor Crater. It is a rotationally

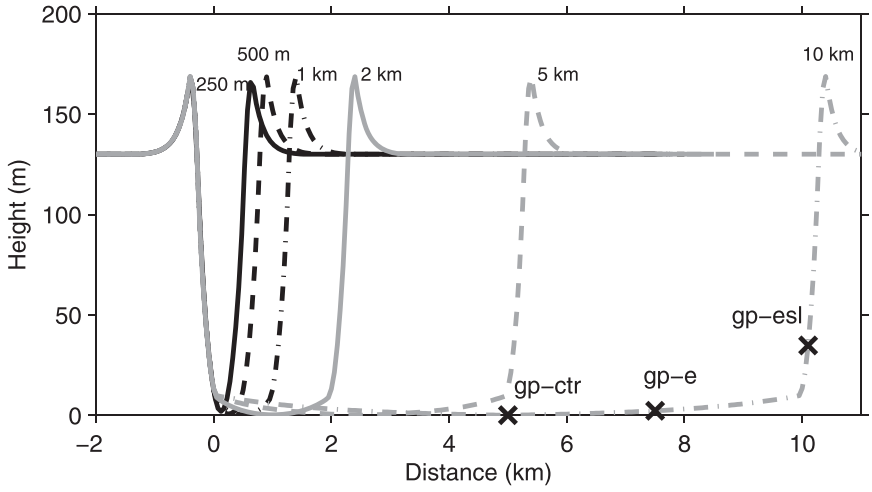

FIG. 2. Cross sections through model topographies with basin-floor widths of 0.25, 0.5, 1, 2, 5, and 10 km. Black crosses indicate the locations of grid points gp-ctr, gp-e, and gp-esl in the 10-km basin.

symmetric, bowl-shaped basin with a floor-to-rim depth of ≈170 m. Simulations are run with different basin-floor widths of 0.25, 0.5, 1, 2, 5, and 10 km while the slope angle is kept approximately constant. Cross sections through all six basins are shown in Fig. 2.

The model domain covers approximately 15 km in the horizontal directions (301 u and v grid points on the Arakawa-C grid in the x and y directions, respectively) for simulations with a 0.25–2-km-wide basin. For simulations with a 5- or 10-km-wide basin, the domain covers 20 and 25 km (401 and 501 grid points), respectively. The horizontal grid spacing is $\Delta x = \Delta y = 50$ m. At the lateral grid boundaries, a periodic boundary condition is applied. In the vertical direction, the domain covers a height of 6 km, with 35 vertical levels. The grid spacing is stretched from $\Delta z \approx 10$ m near the surface (i.e., the lowest mass grid point is at ≈5 m) to $\Delta z \approx 920$ m near the top of the domain. Vertical gridpoint distances are only approximate values because WRF uses a terrain-following pressure coordinate in the vertical direction. Mirocha et al. (2010) show that their WRF–LES simulations agree best with expected solutions from similarity theory if they use a grid aspect ratio $\Delta x/\Delta z$ that is between 2 and 4. In our simulations, the ratio is slightly higher, with $\Delta x/\Delta z \approx 5.2$ near the surface. The goal of our simulations, however, is to investigate the sometimes shallow thermally driven flow near the surface, which requires a sufficient number of vertical levels in the lowest part of the atmosphere to resolve the flow properly. This means that the need for an ideal aspect ratio must be balanced by the need for high vertical resolution. Within the lowest ≈180 m (basin depth ≈ 170 m), 11 model levels are used.

b. Model initialization

Temperature is initialized to be horizontally homogeneous with a combination of two smoothed temperature soundings taken at 0600 mountain standard time (MST) 23 October 2006 inside and outside the Meteor Crater (see initial +0-h profile in Fig. 3a). Data from a tethersonde flown from the center of the crater to a height of ≈235 m are used for the lower part of the atmosphere and are complemented by data from a rawinsonde launched in the close vicinity of the crater basin. Observations from the METCRAX field program revealed a pronounced CBF in the morning of 23 October, which indicates that the atmospheric stability on this day was conducive to the formation of CBFs. All simulations are run with a dry atmosphere. For simulations with background wind, wind speed and wind direction are initialized to be horizontally and vertically homogeneous at all heights above 180 m, that is, ≈10 m above the basin rim. The atmosphere inside the basin and within the lowest 50 m above the surrounding plain is initialized with 0 m s^{-1}.

c. Model physics and parameterizations

A large time step (as opposed to the small acoustic time step) of 0.5 s is used. Coriolis force is neglected because of the small model domain. The ''Noah'' land surface model (Chen and Dudhia 2001) is used in combination with the eta surface layer scheme (Janjić 1994), which is based on Monin–Obukhov similarity theory, to calculate momentum fluxes from the ground to the atmosphere. The kinematic heat flux H is prescribed at the surface as a function of time and terrain as detailed in

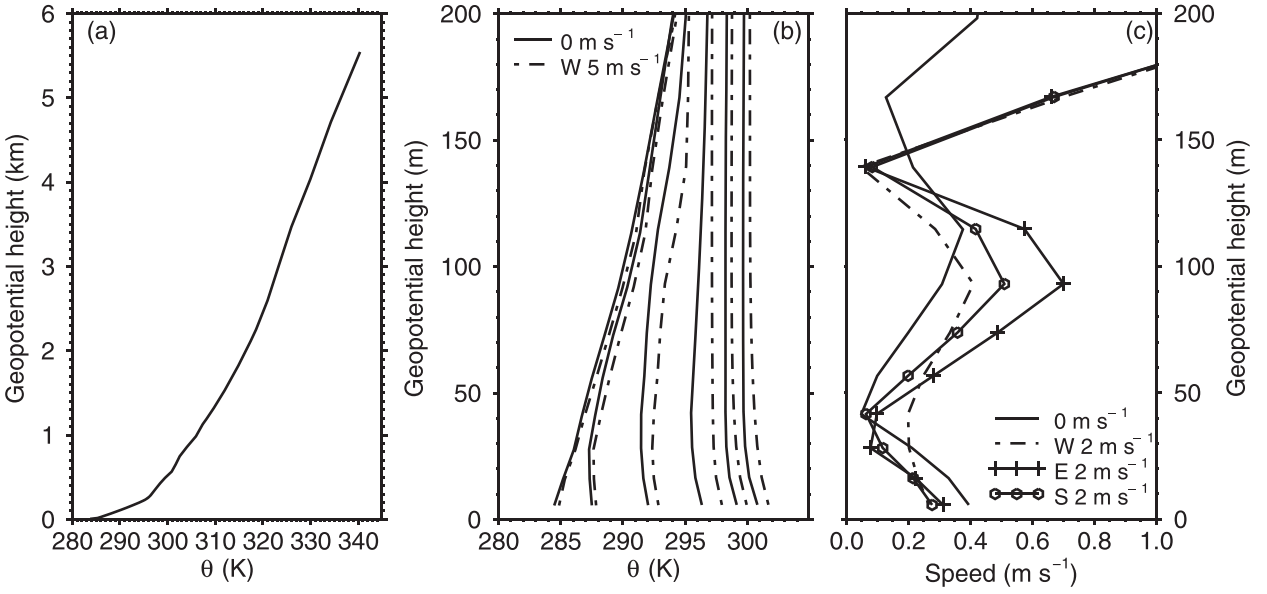

FIG. 3. Vertical profiles in the center of the 500-m basin of (a) initial potential temperature θ profile at +0.0 h; (b) potential temperature for 0 and 5 m s^{-1} westerly background wind at +1.0, +2.0, +3.0, +4.0, +5.0, and +6.0 h (from low to high θ values); and (c) horizontal wind speed for 0 m s^{-1} background wind and 2 m s^{-1} westerly, easterly, and southerly background winds at +3.0 h. Note the different height scale in (a).

the following paragraph. The simulations are run for 6 h. By this time, the basin atmosphere is well mixed and no further information is gained from the simulations.

The heating (i.e., a positive H) is turned on after 1 h of simulation time; during the first hour H is set to zero. A sine function is used to describe the temporal variation of H on a flat surface, with an amplitude of 0.15 K m s^{-1} and a period τ of 24 h $\{H_{\text{plane}} = 0.15 \text{ K m s}^{-1} \times \sin[(t - 1)\pi/\tau]\}$, where t is simulation time in hours. The amplitude of 0.15 K m s^{-1} is representative of observed values at the Meteor Crater (≈111°W, ≈35°N) in October. Since the simulations are run for 6 h but the maximum on the horizontal surface would be reached after 7 h of simulation time, H increases throughout the simulation period. The temporal evolution of H is thus representative of the morning period before noon. For surfaces that are not horizontal, H is a function of slope inclination and orientation, similar to the effect of slope orientation on the incoming solar radiation. The kinematic heat flux at any grid point is given by

$$H = H_{\text{min}} + (H_{\text{plane}} - H_{\text{min}}) \cos i/\cos\delta_{\text{max}},$$

where $H_{\text{min}} = 0.05H_{\text{plane}}$ is a minimum kinematic heat flux that is applied at every grid point, independent of the slope inclination and orientation, similar to the effect of diffuse radiation in shaded areas. The numerator $\cos i = \cos\delta \cos\delta_{\text{max}} + \sin\delta \sin\delta_{\text{max}} \cos(90° - \alpha)$, where δ is the slope angle and α is the azimuth angle. The heat flux is thus distributed so that the maximum possible H at any given time would be on the west sidewall (facing directly east), where $\alpha = 90°$, at a slope angle of $\delta_{\text{max}} = 60°$. Because the maximum slope angle of the basin sidewalls is ≈35°, however, the actual H is smaller than the maximum possible H throughout the basin. The resulting heat flux distribution yields a maximum on the west sidewall and a minimum on the east sidewall. The locations of the local maximum and minimum do not change with time.

The subgrid-scale model used to parameterize the effects of the small, unresolved turbulent motions is the WRF 1.5-order turbulent kinetic energy scheme. Catalano and Moeng (2010) suggest applying a correction function to the isotropic filter length scale based on Scotti et al. (1993) to take into account the strong anisotropy of the grid ($\Delta x/\Delta z \gg 1$). Here, we use instead the standard WRF anisotropic diffusion option, which calculates separate horizontal and vertical length scales. Tests with more vertical grid points, that is, weaker grid stretching, and isotropic diffusion had very little effect on the results. An explicit, 6th-order numerical diffusion (Knievel et al. 2007) is used to dampen 2-Δx waves, and, in the vertical direction a Rayleigh damping layer is applied to the topmost 1 km.

d. Analysis and time averaging

Thermally driven cross-basin winds are a phenomenon of the mean wind. Many previous LES studies derived the

mean flow field from spatial and/or temporal averages, either in both the x and y directions for simulations over homogeneous terrain (e.g., Smith and Skyllingstad 2005; Axelsen and van Dop 2009) or only in one direction over two-dimensional terrain (e.g., Catalano and Moeng 2010). The three-dimensionality of our topography makes spatial averaging impossible and thus necessitates temporal averaging. Because of data storage restrictions the model-field output frequency is limited. Three-dimensional model fields were output every 5 min and then averaged over 0.5-h intervals. The time given in the figures and the text always indicates the end of the averaging period. Because of the small sample size of only 6 values, some fields show indications of turbulent motions even after averaging. Additional time series were output at every time step (0.5 s) for five near-surface (first model level) grid points in the center of the basin (gp-ctr) and at locations along the north (gp-nsl), south (gp-ssl), west (gp-wsl), and east (gp-esl) sidewall and then were averaged over 10-min intervals. Grid points gp-ctr and gp-esl in the 10-km basin are shown in Fig. 2. The heights above the basin floor of gp-nsl, gp-ssl, and gp-wsl are identical to the height of gp-esl in the rotationally symmetric basin and are approximately 35 m in all basins.

e. Comparison of model results with observational data

Before continuing with the analysis of the simulations, we want to verify the model results. For this purpose, results from the simulation with the 500-m basin and no background wind are compared with data from the METCRAX field campaign (Fig. 4). The observational data in Fig. 4 are mean values for the period from 1 to 30 October 2006 after filtering to remove data for background winds exceeding 4 m s^{-1} at the basin rim. A detailed description of the data analysis and the CBF and cross-basin differences in the Meteor Crater can be found in Lehner et al. (2011). Sunrise at the Meteor Crater occurred at about 0700 MST on the west sidewall during October. Thus, the 6-h simulation period is compared with the morning period from 0600 to 1200 MST so that the time of sunrise corresponds to +1.0 h, that is, the time when the surface heat flux is turned on in the model. The curve for the east–west heat flux difference in the Meteor Crater ends slightly before 1200 MST because of missing data after this time. Overall, the model-produced cross-basin heat flux, temperature, and pressure differences and the wind in the center of the basin compare well to the observations. After 1000 MST (+4.0 h) the model starts to deviate slightly from the observations because of the larger heat flux difference in the model, which leads to a stronger pressure difference and CBF. This is not surprising considering that in the Meteor Crater the direction of the horizontal gradients does not stay constantly in an east–west direction but changes continuously as the sun moves across the sky. Until about 0900 MST, the modeled east–west temperature difference compares best to the observed temperature difference that was measured 5 m above the surface, which agrees with the height of the first model level. While the difference in the observations decreases or changes sign, the modeled difference continues to increase in agreement with the increasing heat flux difference so that it then compares better to the temperature difference measured at 5 m above the surface.

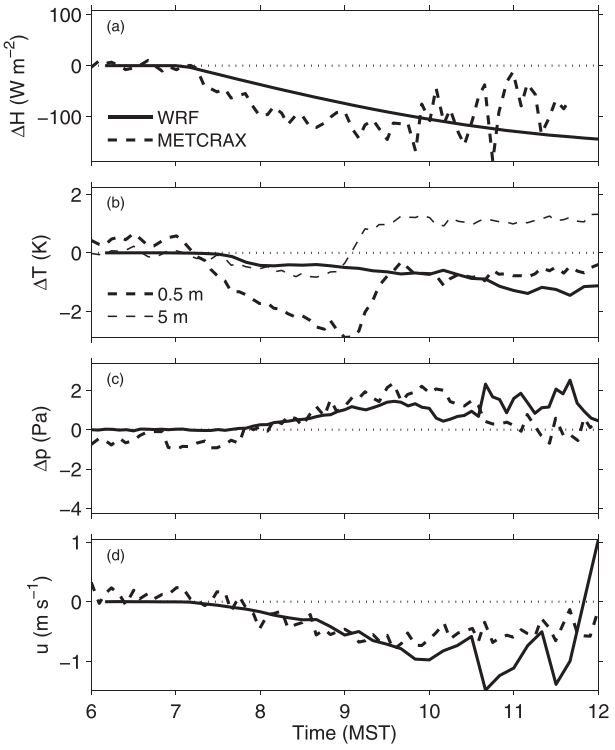

FIG. 4. Comparison of WRF output with observational data from the METCRAX field campaign: (a) heat flux difference between the east and west basin sidewalls, (b) east–west temperature difference, (c) east–west pressure difference, and (d) east–west wind component in the center of the basin. WRF differences are calculated between gp-esl and gp-wsl; u in (d) is at gp-ctr. The time series are taken at the first model level, i.e., ≈5 m above the surface. Heat flux and temperature differences are 10-min averages from 0.5-s time series output; pressure differences are 5-min instantaneous values. METCRAX data are averaged over a 1-month period; pressure and wind measurements were taken at 2 m above ground level.

3. Background wind

Thirteen simulations were performed for the 500-m-wide basin with different background-wind speeds and directions. Wind direction varied from west (opposing

the horizontal heat flux gradient $\nabla_h H$) to south (perpendicular to $\nabla_h H$) and east (parallel to $\nabla_h H$). Four simulations with wind speeds of 1, 2, 3, and 5 m s^{-1} were run for all three wind directions, plus one simulation with 0 m s^{-1} background wind (Fig. 1).

a. General evolution of the basin atmosphere

The development of the temperature structure in the basin is very similar for all simulations (see, e.g., the potential temperature profiles for 0 and 5 m s^{-1} westerly background winds in Fig. 3b). Mixing is slightly stronger for higher background-wind speeds, causing higher temperatures within the basin. The stronger mixing also produces an earlier neutral basin atmosphere; for example, 5 m s^{-1} westerly background winds produce a mixed layer at the top of the basin already at +3.0 h and a completely mixed basin atmosphere above the shallow superadiabatic layer at +4.0 h. The interaction of the background wind and the thermal cross-basin circulation will be compared for the stable, decoupled basin atmosphere (from ≈+1.0 to +3.0 h) and the unstable, coupled atmosphere (after ≈4.0 h).

Examples of the three-dimensional wind field inside the basin are shown at +3.0 h for the 0 m s^{-1} and all three 2 m s^{-1} background-wind cases in Fig. 5. This time corresponds to the last averaged output time at which the surface CBF has not ceased in any simulation (section 3b). The 2 m s^{-1} background-wind speed shows the developing circulation pattern best and is representative of patterns at other background-wind speeds. Higher background winds usually produce also stronger winds inside the basin and a deeper penetration of the background-wind-induced circulation.

Upslope winds form along the greater part of the basin sidewall and are strongest on the west sidewall (lowest u and highest w values; see, e.g., 0 m s^{-1} in Fig. 5). Upslope winds at the west sidewall (at gp-wsl), which receives maximum heating, are mostly persistent throughout the entire simulation period independent of the background-wind direction for background-wind speeds of 3 m s^{-1} or lower (not shown). On the east sidewall (at gp-esl), which receives minimum heating, winds vary more strongly with a less steady upslope flow. At gp-nsl and gp-ssl constant upslope winds occur for wind speeds of 2 m s^{-1} or lower. The upslope flow is compensated by subsidence throughout the basin.

Without a background wind, the strongest subsidence (sinking motions of greater than 5 cm s^{-1}) occurs in the lower part of the basin, where upslope winds occur above most of the sidewalls and the basin cross section is smallest. An easterly CBF is present in the lowest levels, with a westerly RF above ≈50 m. The maximum RF (at the 100-m level) is shifted to the west sidewall, where stronger subsidence occurs. This area also contains the strongest v components away from the slope. The circulation pattern in the completely thermally driven case is thus characterized by upslope winds along the sidewalls, an easterly CBF near the basin floor with a deep westerly RF aloft, and a slope-following, downward directed flow above the upslope-wind layer, which feeds into the CBF.

With a westerly background wind, which opposes the CBF and is parallel to the RF, the CBF layer becomes deeper than 100 m with the strongest easterly winds near the top. The westerly RF above the CBF changes continuously into the westerly background wind. Also, the region of strongest v components away from the slope is shifted toward the east relative to the no-wind case. Rising motions in the west part of the basin and increased subsidence near the center indicate the presence of a closed clockwise-rotating circulation near the basin top, induced by the background wind. The lower, easterly branch of this circulation thus enhances the thermally driven CBF in depth and strength, and the westerly background flow aloft replaces the thermal RF. The size and the exact location of the background-wind-induced vortex vary with background-wind speed. It is difficult to determine a rule for these variations from the simulations, however, except that for 5 m s^{-1} background winds the circulation cell shows an additional downward motion in the along-flow direction in the center of the vortex, which splits the upward motion of the vortex into two parts (see, e.g., 5 m s^{-1} westerly background wind in Fig. 5).

With an easterly background wind, which is parallel to the CBF and opposes the RF, the easterly CBF is again confined to the lower part of the basin. The westerly RF, however, is more strongly developed than in the purely thermal case (see the 100-m level in Fig. 5). Similar to westerly background winds, positive w components in the upper part near the east sidewall indicate the presence of a, in this case, counterclockwise-rotating circulation cell at the top of the basin. The thermal circulation at the basin floor and the background-wind-induced circulation at the top thus form two counterrotating cells with a strong RF in the center.

A comparison of the horizontal wind speed in the center of the basin for different wind directions (Fig. 3c) confirms that wind speeds between 50 and 150 m are weakest without a background wind, that is, with only thermal forcing. For 2 m s^{-1} background winds, the highest wind speeds are produced for easterly background winds, with the thermal and the background-wind forcing pointing in the same direction. Lowest wind speeds occur for westerly background winds, with the thermal and the background-wind forcing opposing

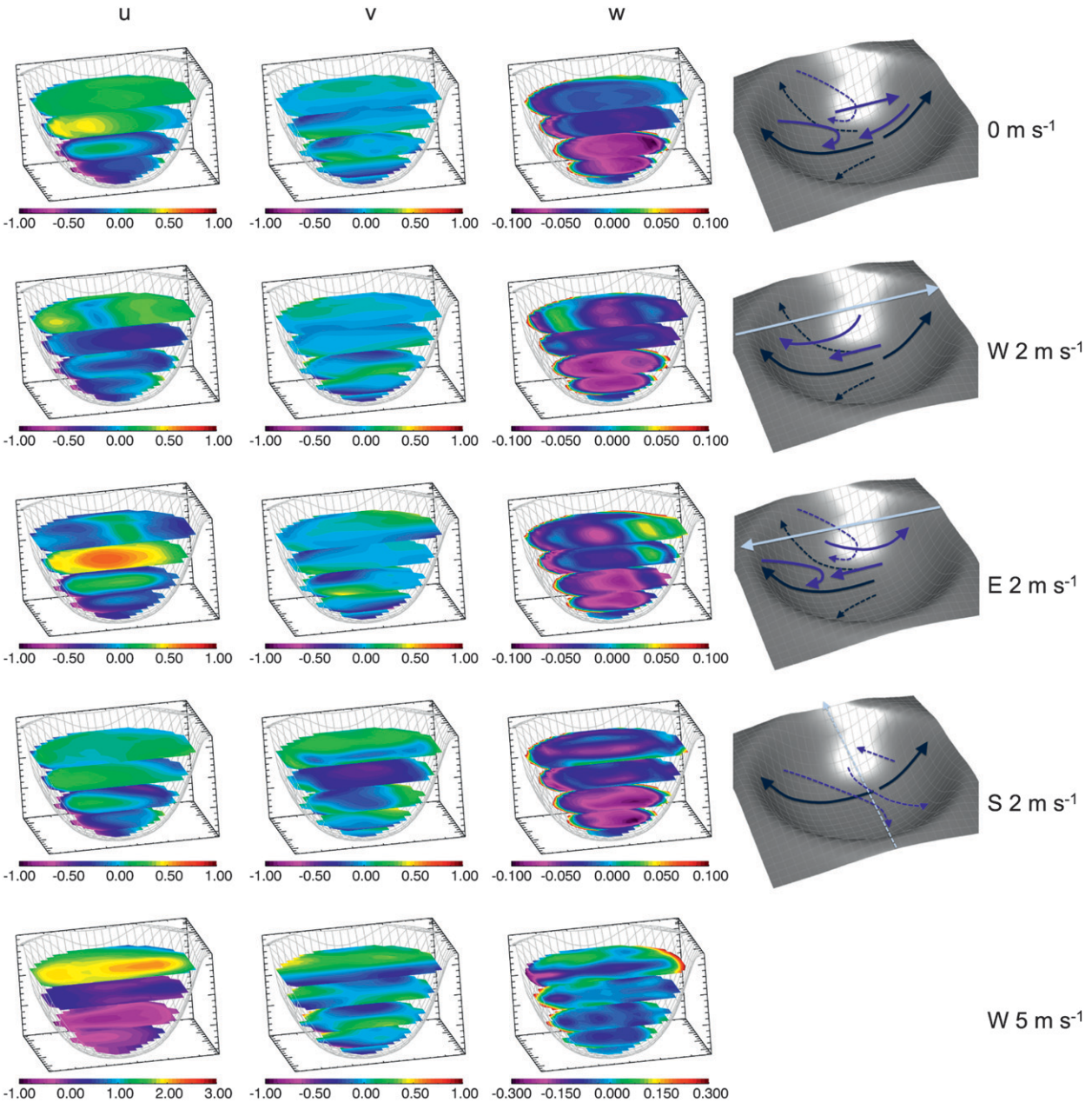

FIG. 5. Horizontal cross sections of (left) u, (left center) v, and (right center) w wind components at 10, 30, 60, 100, and 140 m and (right) schematic diagrams of the wind circulation at +3.0 h for (top) 0 m s^{-1} background wind; 2 m s^{-1} (top middle) westerly, (middle) easterly, and (bottom middle) southerly background winds; and (bottom) 5 m s^{-1} westerly background wind. Note the different scales for the 5 m s^{-1} background-wind case. Black arrows in the schematic diagrams indicate surface winds, blue arrows indicate winds in the basin, and light blue arrows indicate background winds above the basin. Solid arrows indicate winds along an east–west cross section, and dashed arrows indicate winds off to the north and south (0 m s^{-1}, W 2 m s^{-1}, and E 2 m s^{-1}) or at an angle to the east–west cross section (S 2 m s^{-1}).

each other. Wind speeds for southerly background winds lie between these cases, with the thermal and the background-wind forcing along different axes.

With a southerly background wind, which is perpendicular to both the CBF and the RF, the circulation becomes less symmetrical with respect to the east–west axis. The axis of lowest CBF speeds near the basin floor is shifted slightly to an east-southeast–west-northwest direction, and the area of maximum subsidence is confined to the southeastern part of the basin. The u component

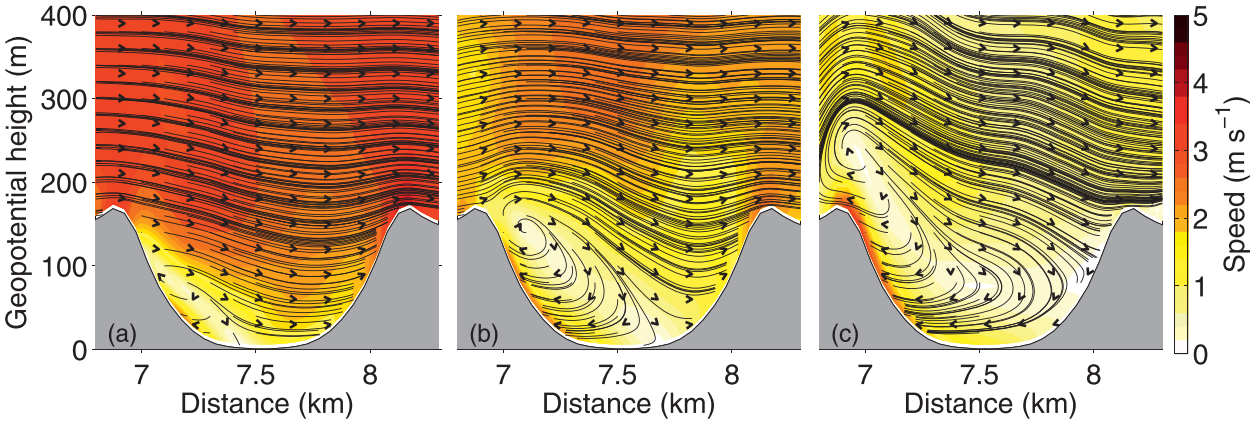

FIG. 6. Streamlines of the wind field along an east–west vertical cross section through the center of the basin at +5.0 h for (a) 3, (b) 2, and (c) 1 m s^{-1} westerly background wind. Black arrowheads indicate the wind direction, and color shading gives the wind speed in the vertical plane.

at 60 m, however, is asymmetric with respect to the northwest–southeast axis with a deeper CBF layer in the northeastern part as compared with the rest of the basin. The circulation above ≈100 m is mostly characterized by the north–south-rotating, background-wind-induced cell, as well as the RF of the thermal circulation, which leads to a shift of the originally westerly RF to a more northwesterly direction.

Stronger background winds start to influence the surface winds at the basin floor earlier than weaker background winds because of stronger shear mixing from above (Fig. 3b). For a 5 m s^{-1} background wind, surface winds show a component in the direction of the background wind throughout the basin at +4.0 h. This includes downslope winds on the west sidewall for westerly background winds. For 3 m s^{-1} westerly background winds, the greater part of the basin atmosphere shows westerly winds by this time. The thermal circulation still prevails within a shallow layer close to the surface on the west sidewall, forming a small eddy (Fig. 6a). This eddy near the west sidewall grows with decreasing background-wind speeds, spanning the entire western half of the basin for 2 m s^{-1} (Fig. 6b) and almost the entire basin and reaching up to a height of ≈300 m for 1 m s^{-1} background winds (Fig. 6c). A similar, but much smaller, eddy forms in the lee of the upstream rim for easterly background winds of 1 and 2 m s^{-1} (not shown). In this case, the heating on the east sidewall is insufficient to produce a strong upslope flow and a large eddy comparable to that produced on the west sidewall with westerly background winds. For southerly background winds, the circulation with respect to the north–south axis is almost symmetric with a slightly stronger circulation cell in the western part due to the cross-basin temperature gradient. In the north–south direction, however, the circulation is very similar to the circulation in the east–west direction for westerly background winds. This suggests that in the neutral atmosphere the wind field within the basin is mainly determined by the background wind so that the thermal CBF plays only a minor role.

b. CBF and RF characteristics

After the onset of heating at +1.0 h, surface (i.e., at the first model level) winds at the basin center turn to a constant easterly direction, with wind speeds increasing with time (Fig. 7). This initial development during the first ≈2 h after the onset of heating, when the basin is decoupled from the atmosphere aloft, is almost identical for all simulations. Variations in u are slightly stronger for higher background-wind speeds of 3 and 5 m s^{-1}, but CBF speeds still have a similar magnitude. After +3.0 h, when the basin atmosphere is close to neutral, surface winds become more variable and increase strongly in magnitude. Whereas surface u remains mostly easterly with a trend to increasing wind speeds with time for background winds of 2 m s^{-1} or less, surface u for background winds of 3 m s^{-1} or more changes suddenly and then remains mostly constant with slight variations for the rest of the simulation period.

Onset times of the surface CBF were determined from the time series output at gp-ctr with a resolution of 10 min (Fig. 8). The onset is defined as the time at which the surface u component becomes lower than −0.1 m s^{-1} (negative values denote easterly winds) after +1.5 h. The additional 0.5 h after the onset of heating avoids the early period of very weak and varying winds. The earliest onset is +1.5 h for a 5 m s^{-1} westerly background wind, whereas the latest onset is +2.0 h for easterly background winds of 2 m s^{-1} or more. This result suggests that easterly background winds can dampen the onset of

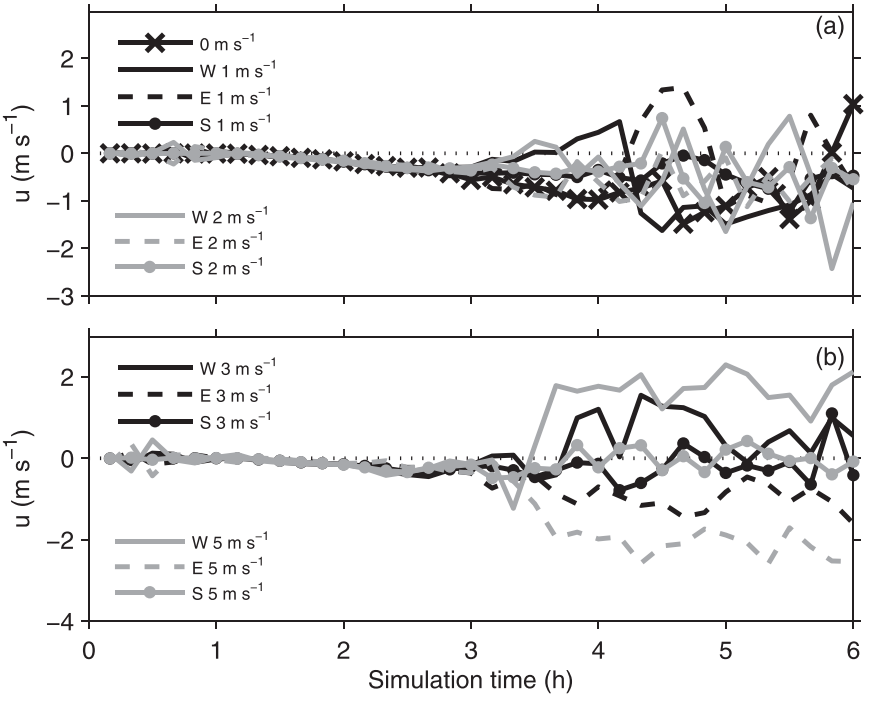

FIG. 7. Time series of surface u wind components in the center of the 500-m-wide basin for all simulations with (a) 0–2 m s^{-1} and (b) 3 and 5 m s^{-1} background wind.

the thermally driven CBF at the basin floor even though the basin atmosphere is stably stratified. The damping seems to be caused by vertical momentum transport from the westerly and thus CBF-opposing flow in the lower branch of the background-wind-induced circulation cell. In a similar way, a westerly background wind seems to accelerate the onset slightly relative to easterly and southerly winds. For southerly background winds, the onset is identical to the 0 m s^{-1} case, with an onset time of +1.83 h except for 3 m s^{-1} background wind.

Further CBF and RF characteristics were determined for every half hour from vertical profiles at the center of the basin floor (gp-ctr) and four grid points located halfway between gp-ctr and the north (gp-n), south (gp-s), east (gp-e), and west (gp-w) sidewalls, respectively (see the location of gp-e in the 10-km basin in Fig. 2). The parameters include CBF surface wind speed; CBF layer depth; CBF maximum below the top of the CBF layer or below 200 m, whichever is lower; the height at which the maximum occurs; RF layer depth; RF maximum between the bottom and the top of the RF layer or 200 m, whichever is lower; and the height at which the RF maximum occurs. These parameters are only defined if the surface u at the respective time shows an easterly wind component. Furthermore, all parameters characterizing the RF are only defined if the RF starts at a height lower than 200 m, because we are only interested in an RF in or directly above the basin. The CBF layer is defined as the layer with an easterly wind component directly above the surface. Its top corresponds to the height of the last grid point where an easterly wind component occurs and is topped by the RF with a westerly wind component. Table 1 summarizes the above parameters at gp-ctr at +1.0, +3.0, and +5.0 h, which represent the atmosphere before the onset of heating, during the stable regime, and during the neutral regime, respectively.

A comparison of the five locations shows that CBF and RF characteristics are very similar at gp-n and gp-s for westerly and easterly background winds, particularly

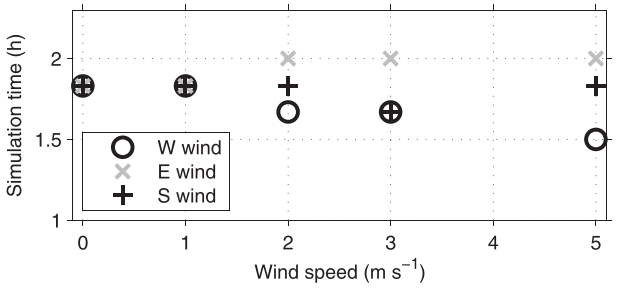

FIG. 8. Surface CBF onset time (see text for definition) in the center of the 500-m basin for different background-wind speeds and background-wind directions.

TABLE 1. CBF and RF characteristics for different background-wind speeds and background-wind directions at gp-ctr. Values are given at +1 h (onset of heating), +3 h (basin atmosphere decoupled from the atmosphere aloft), and +5 h (basin atmosphere coupled to the atmosphere aloft). Dashes indicate values that are not defined; bw stands for background wind, indicating that the CBF or RF is coupled to the background wind with the same wind direction so that its depth cannot be determined. See text for more information.

		West (W) wind (m s^{-1})				East (E) wind (m s^{-1})				South (S) wind (m s^{-1})			
Time (h)	0 m s^{-1}	1	2	3	5	1	2	3	5	1	2	3	5
CBF surface speed (m s^{-1})													
+1	—	0.02	0.03	0.02	0.07	—	—	—	—	—	—	—	—
+3	0.4	0.26	0.27	0.23	0.07	0.43	0.31	0.34	0.32	0.35	0.27	0.21	0.21
+5	1.18	1.18	0.82	—	—	—	0.53	1.12	1.63	0.11	0.49	0	—
CBF depth (m)													
+1	—	6	6	6	41	—	—	—	—	—	—	—	—
+3	42	115	115	93	93	28	28	28	16	28	28	42	57
+5	58	75	43	—	—	—	bw	bw	bw	323	375	6	—
CBF max (m s^{-1})													
+1	—	0.02	0.03	0.02	0.07	—	—	—	—	—	—	—	—
+3	0.4	0.26	0.41	0.46	0.67	0.43	0.31	0.34	0.32	0.35	0.27	0.21	0.21
+5	1.18	1.18	0.82	—	—	—	bw	bw	bw	0.16	0.49	0	—
Height of CBF max (m)													
+1	—	6	6	6	6	—	—	—	—	—	—	—	—
+3	6	6	93	74	74	6	6	6	6	6	6	6	6
+5	6	6	6	—	—	—	bw	bw	bw	95	6	6	—
RF depth (m)													
+1	—	0	0	0	0	—	—	—	—	—	—	—	—
+3	82	bw	bw	bw	bw	97	98	73	65	125	232	177	41
+5	126	bw	bw	—	—	—	—	—	—	—	—	154	—
RF max (m s^{-1})													
+1	—	0.01	0.04	0	0.06	—	—	—	—	—	—	—	—
+3	0.38	bw	bw	bw	bw	0.52	0.7	0.66	0.74	0.27	0.19	0.09	0.18
+5	0.21	bw	bw	—	—	—	—	—	—	—	—	0.13	—
Height of RF max (m)													
+1	—	16	16	16	56	—	—	—	—	—	—	—	—
+3	114	bw	bw	bw	bw	93	93	93	74	93	93	74	93
+5	95	bw	bw	—	—	—	—	—	—	—	—	117	—

before +4.0 h, and thus that the development of the CBF and RF in the stable atmosphere is approximately symmetrical with respect to the east–west axis (not shown). With southerly background winds, values at gp-n and gp-s start to differ earlier and more strongly, particularly for RF characteristics because of the stronger influence of background winds near the top of the basin. Throughout most of the simulation the CBF is stronger and more persistent at gp-w than at gp-ctr and is weaker and often not defined at gp-e. Only with easterly background winds does a more persistent easterly wind develop at gp-e after ≈+3.0 h, with values of more than 1 m s^{-1} for the 5 m s^{-1} background-wind speeds. This is an indication of easterly background winds being mixed down to the surface. With westerly background winds, nonthermal easterly surface winds with values of 0.02–0.07 m s^{-1} are already present at gp-ctr at +1.0 h (Table 1). Half an hour later, however, CBF speeds are relatively independent from the background wind, at 0.02–0.04 m s^{-1}.

Simulations with easterly background winds give an estimate of the time at which the surface winds become coupled to the background wind above the basin. At that time the CBF makes a sudden transition into the background wind having the same wind direction so that the depth of the CBF can no longer be determined (denoted by "bw" in Table 1). Coupling occurs between +3.0 and +5.5 h depending on the location within the basin and on the background-wind speed, with higher wind speeds being mixed down faster than weaker winds. Of interest is that the CBF layer for easterly background winds seems to grow faster to the north and south of the center between +2.0 and +3.0 h, and then the depth decreases again slightly before the CBF couples to the background wind. For westerly background winds, however, the CBF layer grows more slowly away from the center, that is, at gp-s, gp-n, and gp-w (except for the 5 m s^{-1} case at gp-w); the CBF is deeper at gp-e if it is present. A possible explanation is that the effect of the background-wind-induced circulation (enhancing for westerly winds and damping for easterly winds) decreases with distance to the north and south.

In the case of easterly background winds, in which two counterrotating cells form, the CBF maximum values

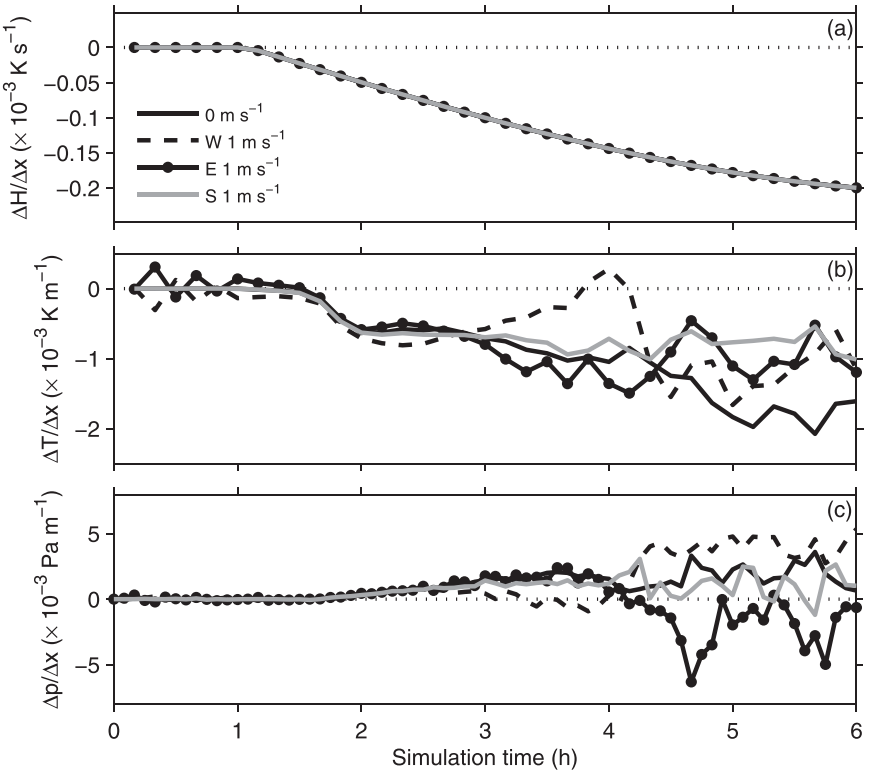

FIG. 9. East–west (a) heat flux, (b) temperature, and (c) pressure gradients between gp-esl and gp-wsl in the 500-m wide basin for 0 and 1 m s^{-1} west, east, and south background wind. Heat flux and temperature gradients are 10-min averages from 0.5-s time series output; pressure gradients are 5-min instantaneous values.

are mostly reached at the surface throughout the basin. For westerly background winds the CBF maximum is reached more often away from the surface as background-wind speeds increase. The maximum height is connected to the depth of the CBF layer, since it has to occur within that layer. Thus, the CBF maximum is reached at higher levels during the first few hours for simulations with strong westerly background wind because the CBF layer grows faster.

According to its definition, the RF starts at the first model level above the CBF layer. If the CBF layer, however, is deeper than 200 m then the RF is not defined. Similar to the CBF depth for easterly background winds, the RF depth for westerly background winds reveals the coupling of the RF to the background wind (denoted by bw). Because the CBF layer at gp-ctr grows more rapidly for higher winds speeds, the top of the RF also reaches the downward-growing layer of westerly winds more quickly. For 3 and 5 m s^{-1} the coupling occurs already within the first half hour after the onset of heating. At gp-n and gp-s, on the other hand, the coupling occurs only between +2.5 and +3.0 h, independent of the background-wind speed. The RF layer for southerly background winds becomes deeper (up to ≈230 m at gp-ctr) than the RF layer for easterly background winds, which oppose the RF.

The RF attains maximum values of up to ≈0.7 m s^{-1} at gp-ctr for easterly and ≈0.4 m s^{-1} for southerly background winds. For westerly background winds, however, the RF, which makes a transition directly into the background flow, shows higher maxima with up to ≈3.4 m s^{-1} at gp-ctr for 5 m s^{-1} background winds. In a similar way, RF maxima are obtained at lower heights for easterly background winds (below 120 m), whereas maxima for southerly and westerly background winds are reached at heights of up to ≈200 m.

c. *Thermal CBF forcing*

The magnitude of the east–west temperature gradient $|\Delta T/\Delta x|$, calculated between gp-esl and gp-wsl, increases quickly from $\approx 0.06 \times 10^{-3}$ K m^{-1} at +1.5 h to $\approx 0.6 \times 10^{-3}$ K m^{-1} at +2.0 h (e.g., Fig. 9b for 0 and 1 m s^{-1} background winds). Without a background wind, $\Delta T/\Delta x$ is mostly a function of the heat flux gradient $\Delta H/\Delta x$ (Fig. 9a), with an almost linear relation (not shown). Only in the neutral basin atmosphere after ≈4.0 h do values

deviate more strongly from a linear curve. The temperature gradient stays negative throughout the entire simulation period for all 1 m s^{-1} background-wind simulations except for a short period in the case of westerly background winds, in which $\Delta T/\Delta x$ starts increasing at $\approx+2.5$ h and reaches its peak at +4.0 h before it drops again. Similar sudden increases (westerly background wind) or decreases (easterly background wind) in $\Delta T/\Delta x$ or increases in $\Delta T/\Delta y$ (southerly background wind) occur also in all other background-wind cases except for 1 m s^{-1} easterly winds. With higher wind speeds, the temperature gradient peaks earlier, for example, at +3.0 h for 5 m s^{-1} background winds. A faster downward growth of the mixed layer aloft on the downstream basin side and thus an earlier coupling with the growing mixed layer in the basin results in stronger surface temperature increases on the downstream sidewall and these sudden changes in the cross-basin temperature difference. Except for these short periods, $\Delta T/\Delta x$ is relatively constant after +2.0 h with $\approx-1.0\times10^{-3}$ K m^{-1}, independent of background-wind direction and speed. Of interest is that the maximum $|\Delta T/\Delta x|$ reached at the end of the simulation period is generally weaker with background winds when compared with no background wind (e.g., 1 m s^{-1} in Fig. 9b). This suggests stronger horizontal mixing in the basin in the presence of background winds.

The east–west pressure gradient $\Delta p/\Delta x$ becomes positive after the onset of heating and increases with time, independent of the winds above rim level. Once the basin atmosphere is coupled to the atmosphere aloft, $\Delta p/\Delta x$ seems to be strongly influenced by the background-wind direction even with a comparatively weak background wind of 1 m s^{-1}. This becomes obvious from the opposite signs of $\Delta p/\Delta x$ for easterly and westerly 1 m s^{-1} background winds with positive signs (i.e., higher pressure on the east sidewall) for westerly winds and negative signs (i.e., higher pressure on the west sidewall) for easterly winds (Fig. 9c). In the case of southerly 1 m s^{-1} background winds, however, $\Delta p/\Delta x$ remains slightly positive, similar to the no-background-wind case. This suggests that the simulations with southerly background winds give an estimate of the pressure gradient produced by asymmetric heating. The absolute value $|\Delta p/\Delta x|$ for westerly background winds is mostly higher than for easterly background winds, particularly after +4.0 h, which indicates a combination of thermal and dynamic forcing. Opposing signs of $\Delta p/\Delta x$ for easterly and westerly background winds (and equally a positive $\Delta p/\Delta y$ for southerly background winds) are also produced for higher wind speeds of 2, 3, and 5 m s^{-1}. Despite the negative $\Delta p/\Delta x$ for easterly background winds, an easterly CBF persists throughout most of the simulation period for low background-wind speeds of 2 m s^{-1} or less (Fig. 7a).

4. Basin width

We ran simulations with basin floor widths of 0.25, 0.5 (the same simulation that was discussed as the no-wind simulation in section 3), 1, 2, 5, and 10 km. The shape of the basin sidewalls was kept constant so that the cross-basin heat flux gradient is only a function of the basin width; only the shape of the slightly rising basin floor (a total height difference of 10 m in all simulations) was allowed to vary (Fig. 2). All simulations discussed in sections 4a–c were run with no initial background winds. Additional simulations with background winds are discussed in section 4d.

a. General evolution of the basin atmosphere

The atmosphere in the small basins heats faster than does that in the large basins (Fig. 10a). Temperature differences are highest between $\approx+3.0$ and +5.0 h (see, e.g., +4.0 h in Fig. 10a). After the basin atmosphere has been completely mixed with the atmosphere aloft, basin temperatures are again similar except for the two largest basins of 5- and 10-km width. Faster heating of the smaller basins implies earlier neutral stratification and coupling to the atmosphere aloft, which is relevant for the impact of background winds on the thermal circulation (section 4d) and which also affects the relative importance of pure CBFs in the stable atmosphere versus turbulent motions in the neutral atmosphere. The atmosphere in the 250-m-wide basin becomes neutral above a shallow superadiabatic surface layer at +4.0 h. In the 5- and 10-km-wide basins a neutral basin atmosphere is reached about 1–1.5 h later.

Three-dimensional wind components at +3.0 h (Fig. 11) indicate that the atmosphere in the 5- and 10-km basins develops differently from that in the smaller basins. Away from the slopes, a cellular structure is present, similar to convection over the plain. The nearly circular arrangement of the convection cells lasts until approximately +3.5 h and is the result of a superposition of the convective cells and weak waves, which originate probably from artificial horizontal pressure gradients near the steep slopes during the first simulation hour. Their existence, however, does not influence the result that convection dominates inside the large basins instead of the cross-basin circulation. A comparison of the wind components at +3.0 h for basin widths of 0.25, 0.5, 1, and 2 km shows that there is little difference among the simulations. In all four simulations a maximum westerly wind component of similar strength is located around 100 m near the west sidewall. The relative area of westerly winds at the 60-m level, however, increases with increasing basin width, suggesting a less deep CBF. Subsidence is generally stronger in the smaller basins because

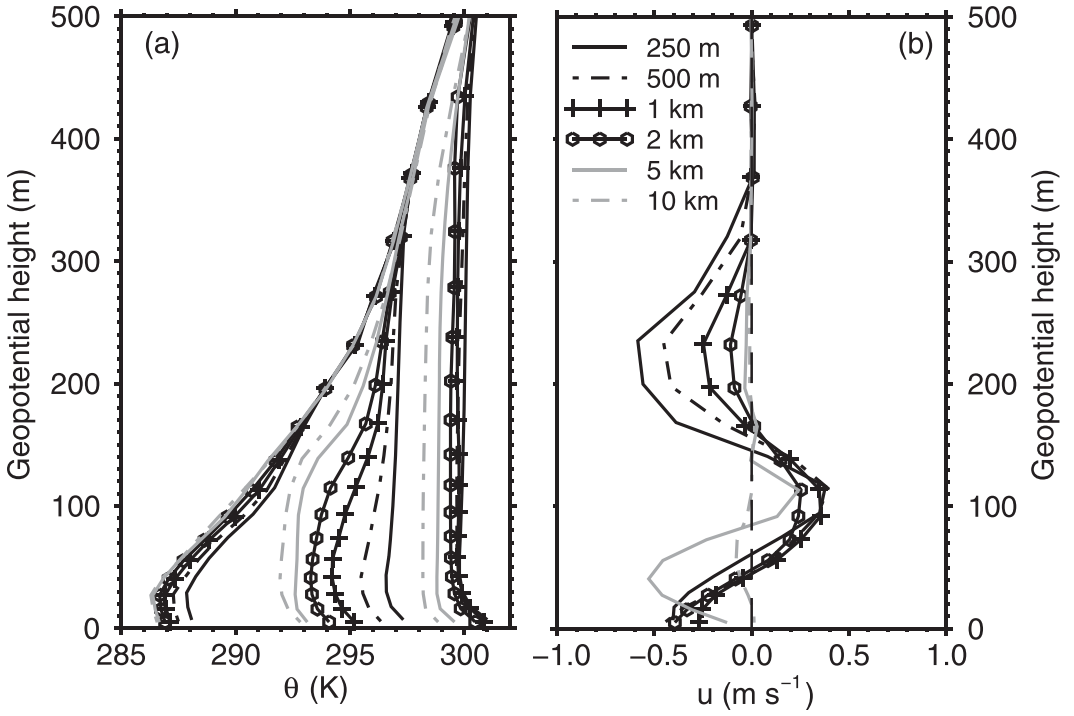

FIG. 10. Vertical profiles of (a) potential temperature at +2.0, +4.0, and +6.0 h and (b) the east–west wind component at +3.0 h in the center of the basin for different basin widths.

of the smaller area that is available to compensate the upslope-flow mass flux, which is in agreement with stronger heating.

b. Thermal CBF forcing

Because the slope angles of the basin sidewalls are kept constant, differences in the surface heat flux, which is a function of slope angle and orientation, are negligible. Small variations occur as a result of the discrete grid points whose locations along the basin topography vary slightly. For instance, the grid points gp-esl and gp-wsl, which were used to calculate the east–west gradients in Fig. 12, were chosen to lie exactly on an east–west line and at an approximate height of 35 m (Fig. 2). The exact height of the individual grid points is 28.7 m (250-m basin), 35.4 m (500 m), 35.1 m (1 km), 34.9 m (2 km), 34.8 m (5 km), and 34.7 m (10 km). The largest difference in surface heat flux among the simulations with different basin widths occurs at gp-esl at +6.0 h, where the heat flux in the 250-m basin is ≈0.1 K m s^{-1} higher than in the other basins.

The CBF in the center of the 500-m-wide basin develops after 1.5–2.0 h (Fig. 8). At this time, $\Delta H/\Delta x$ is between -0.02×10^{-3} and -0.05×10^{-3} K m s^{-1} (Fig. 12a). Maximum $|\Delta H/\Delta x|$ at the end of the simulation period for the 5- and 10-km basins is only slightly higher or even below these values, with −0.027 and −0.014 K m s^{-1}, respectively. This may explain why no or only a weak CBF is produced in these basins. The differences in $\Delta H/\Delta x$ among the simulations are, of course, mostly reflected in $\Delta T/\Delta x$ and $\Delta p/\Delta x$ (Figs. 12b,c). Of interest is that $|\Delta T/\Delta x|$ in the 250-m basin shows strong variations throughout the simulation and after an initially strong increase $|\Delta T/\Delta x|$ is of a similar magnitude and sometimes is even weaker than $|\Delta T/\Delta x|$ in the 500-m basin. The magnitude of the pressure gradient is correspondingly weak. Horizontal warm-air advection on the east sidewall seems to reduce the cross-basin temperature difference initially. After +4.0 h it is vertical warm-air advection at gp-esl that keeps the horizontal temperature gradient low.

c. CBF and RF characteristics

Regardless of basin width, an easterly CBF forms in the center of the basin after the onset of heating at +1.0 h (Fig. 13a). Although none of the entries for the 10-km basin in Table 2 is defined (i.e., no CBF is present at the surface), a CBF does occur between +1.5 and +2.0 h at gp-ctr. CBF wind speeds in the 5- and 10-km basins, however, are very weak, with surface winds of 0.01 m s^{-1} (10 km) and 0.02 m s^{-1} (5 km) at +2.0 h as compared with 0.06–0.18 m s^{-1} in the smaller basins, which agrees with the relatively weak east–west gradients shown in Fig. 12. After +2.0–3.0 h, surface winds

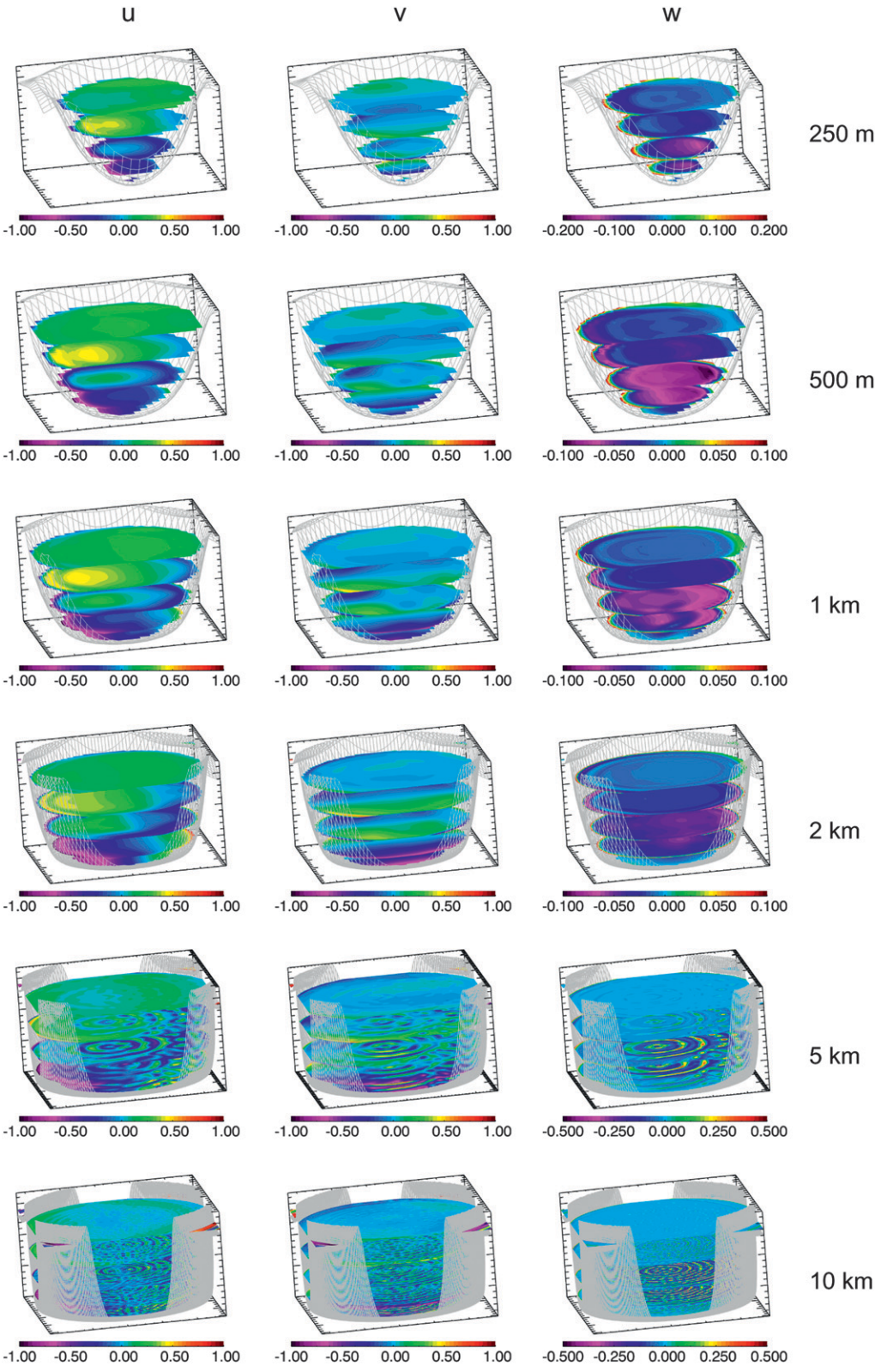

FIG. 11. Horizontal cross sections of (left) *u*, (center) *v*, and (right) *w* wind components at 10, 30, 60, 100, and 140 m for (top to bottom) 250- and 500-m and 1-, 2-, 5-, and 10-km basins. Note the different scales for the *w* wind component for different basin widths.

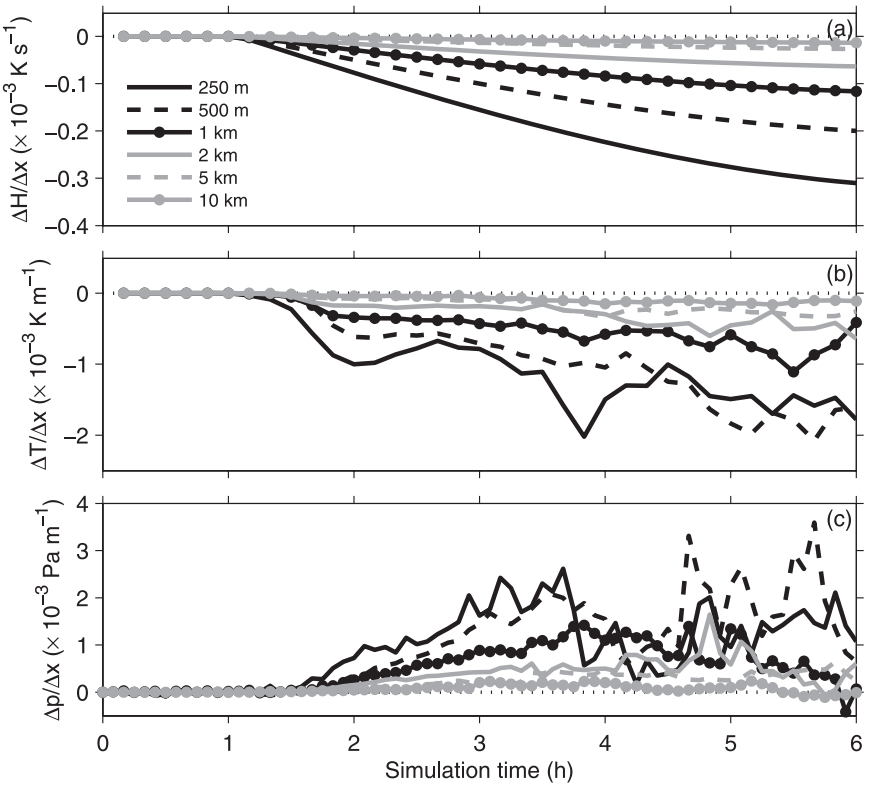

FIG. 12. As in Fig. 9, but for different basin widths and 0 m s^{-1} background wind.

become strongly varying in the 5-km basin and mainly westerly in the 10-km basin, whereas a mostly persistent CBF is present in the smaller basins. This suggests that in the stable atmosphere a weak CBF can form even in basins or valleys on the order of 10 km as a result of a weak pressure gradient. In a less stable atmosphere with increasing turbulence, however, a stronger pressure gradient is necessary to maintain the CBF. Reduced $|\Delta T/\Delta x|$ and $|\Delta p/\Delta x|$ in the 250-m basin are also reflected in u, with a weaker CBF after ≈4.0 h when compared with the larger basins.

The CBF onset time (see definition in section 3b) increases with increasing basin width, occurring between ≈0.5 h (250-m basin) and ≈1.3 h (5 km) after the onset of heating for basin widths of up to 5 km (not shown). Comparing these onset times with $\Delta H/\Delta x$, $\Delta T/\Delta x$, and $\Delta p/\Delta x$, however, does not indicate a certain threshold value above which a CBF forms. There is an indication that for the larger basins the onset of a CBF occurs already at lower absolute heat flux and temperature gradients, with the exception of the 250-m basin. Because the start time is defined as the time at which the easterly surface wind component becomes 0.1 m s^{-1} or larger and all simulations show an easterly component at gp-ctr at +1.5 h (not shown), this delay in wind speed increase may indicate the effect of cumulative forcing, that is, that the CBF speed is determined by the integrated cross-basin forcing over time rather than the current gradients.

The initial CBF layer is deeper the wider the basin is; for example, at +1.5 h the CBF depth at gp-ctr is 17.2 m in the 250-m basin, 40.4 m in the 1-km basin, and 164.4 m in the 5-km basin. Whereas the CBF layer in the smallest basins (250 and 500 m) shows a tendency to grow during the early part of the simulation, it stays approximately constant in the midsized basins (1 and 2 km), and decreases in the widest basins (5 and 10 km). The rate of growth or decrease of the CBF layer varies throughout the basin and the simulation period. At +3.0 h, CBF and RF are similar in strength and depth in all basin widths of 2 km or smaller, however: see, for example, u profiles at gp-ctr in Fig. 10b and Table 2. At this time the CBF has reached a depth of ≈50 m and is topped by an approximately 100-m-deep RF. Above the RF, u changes sign again to an easterly component, which is of a magnitude similar to the CBF in the smaller basins and decreases with basin size (Fig. 10b). The depth of this secondary easterly flow layer also decreases with basin size and is ≈200 m in the 250-m basin. This layer is not present in simulations with background

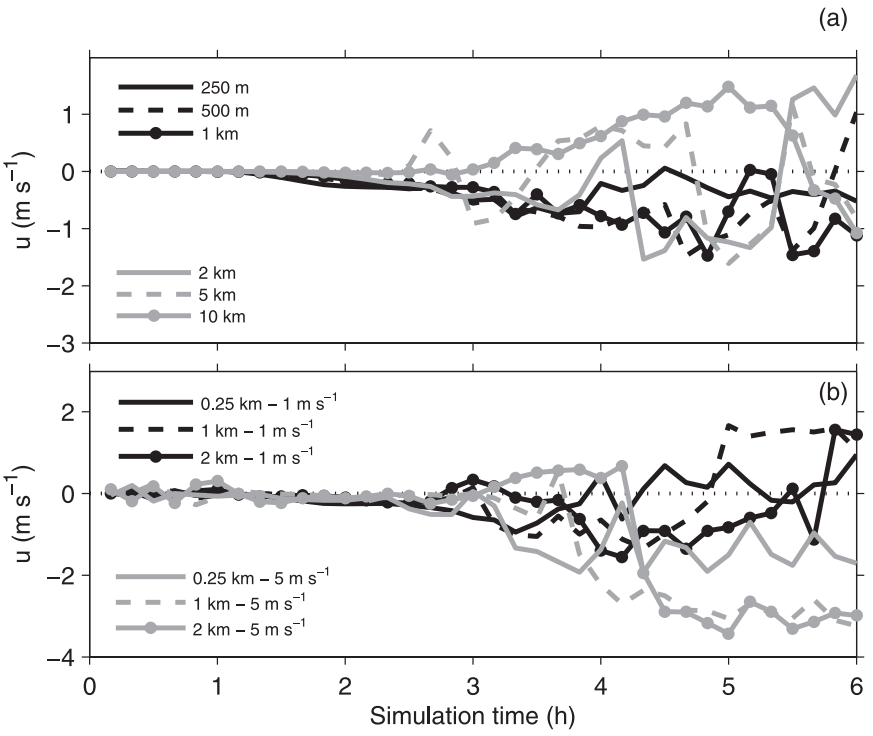

FIG. 13. Time series of surface u-wind component in the center of the basin for different basin widths and (a) 0 m s^{-1} and (b) 1 and 5 m s^{-1} easterly background winds.

winds, in which the wind returns to the background-wind direction and speed above the RF.

The time of RF onset also increases with increasing basin width from +1.5 h (250 m), over +2.0 h (0.5–2 km), to +3.0 h (5 km) at gp-ctr. In the 10-km basin, an RF does not develop at gp-ctr. Maximum RF speeds strengthen during the stable period and are also mostly homogeneous throughout the basin for basin widths of 2 km or smaller. RF wind speeds are less horizontally homogenous (and are often not defined) in the 5- and 10-km basins because of the stronger impact of smaller-than-basin-scale convective cells.

d. Background wind

Additional simulations with 250-m, 1-km, and 2-km basins were run with easterly background winds of 1, 3, and 5 m s^{-1} (Fig. 1). In the stable basin atmosphere the effect of the background wind on the wind profile in the center of the basin is mostly independent of the basin width (Fig. 14a). In the upper part of the basin, where the background wind forms a vortex, the background-wind speed has a stronger impact on the wind profile than does the basin width. A dependence on the basin width, however, occurs around +3.0 h (Fig. 14b). Because the atmosphere mixes faster in the smaller basins and the stability is thus closer to neutral, background winds penetrate farther into the basin, particularly for high background-wind speeds of 3 and 5 m s^{-1}. The RF layer is thus thinner the smaller the basin is.

The surface CBF in the stable atmosphere is affected little by the background winds, regardless of basin width (Fig. 13b). Strong background winds of 5 m s^{-1} that penetrate the basin atmosphere under neutral conditions produce higher surface wind speeds at the basin floor in the wider basins, however (e.g., ≈3 m s^{-1} in the 1-km basin and 1–2 m s^{-1} in the 250-m basin).

5. Discussion and conclusions

Idealized simulations of cross-basin winds were performed using the WRF. The idealized, axisymmetric basin topography was based on the topography of Arizona's Meteor Crater, where cross-basin winds have been observed under quiescent conditions (Lehner et al. 2011). A heat flux that varied with slope inclination and orientation was prescribed at the surface to produce a temperature gradient across the model basin. The direction of the resulting heat flux gradient was constant throughout the simulation period. Simulations were run with varying basin-floor diameters, ranging from 250 m to 10 km, and with varying background-wind speeds (0–5 m s^{-1}) and directions (parallel, perpendicular, and

TABLE 2. As in Table 1, but for different basin widths and 0 m s^{-1} background wind. The 0.5-km simulation is identical to the 0 m s^{-1} simulation in Table 1 but is repeated here for comparison.

	Basin width (km)					
Time (h)	0.25	0.5	1	2	5	10
CBF surface speed (m s^{-1})						
+1	—	—	—	—	—	—
+3	0.34	0.4	0.23	0.37	0.30	—
+5	0.20	1.18	0.84	0.94	0.88	—
CBF depth (m)						
+1	—	—	—	—	—	—
+3	58	42	41	41	73	—
+5	660	58	75	42	74	—
CBF max (m s^{-1})						
+1	—	—	—	—	—	—
+3	0.37	0.4	0.23	0.37	0.56	—
+5	0.20	1.118	0.84	0.94	0.88	—
Height of CBF max (m)						
+1	—	—	—	—	—	—
+3	18	6	5	5	41	—
+5	7	6	5	5	5	—
RF depth (m)						
+1	—	—	—	—	—	—
+3	65	82	82	110	22	—
+5	—	126	142	112	142	—
RF max (m s^{-1})						
+1	—	—	—	—	—	—
+3	0.36	0.38	0.34	0.25	0.21	—
+5	—	0.21	0.46	0.37	0.36	—
Height of RF max (m)						
+1	—	—	—	—	—	—
+3	116	114	114	113	113	—
+5	—	95	169	94	200	—

opposing the heat flux gradient) above the basin. An overview of the regimes that describe the circulation inside the basin depending on the above parameters is given in Fig. 15.

A relatively persistent cross-basin flow develops only in basins that are smaller than 5 km (from 250 m to 2 km). In the larger basins, the thermally driven horizontal temperature and pressure gradients become very small and the development of the basin atmosphere strongly resembles that over the flat plane outside the basin (referred to as *convective regime* in Fig. 15). Convective cells dominate as the air near the surface is heated. In real-world valleys and basins the temperature gradient across the valley or basin depends on many factors besides the distance between the two opposing sidewalls, including the sidewall slope angles and orientations, shading by surrounding topography, the position of the sun, and surface conditions that determine the local energy budget. The order of magnitude of the changes in the temperature gradient due to changes in the local temperature on two opposing sidewalls, however, can be expected to be small relative to the order of magnitude of the changes due to varying valley and basin widths, which can range from several hundred meters to several kilometers. Thus, we conclude that our results are representative for many real valleys and basins.

The forcing for the CBF—that is, horizontal temperature and pressure gradients—generally increases with decreasing basin width. An exception is the 250-m basin, which shows reduced temperature and pressure gradients. The reduced forcing is also reflected in the CBF, which is comparatively weak, so that the strongest CBFs occur in the 500-m-wide basin. The reduced horizontal gradients are a result of warm-air advection across the basin and from the basin floor up the east sidewall. The implication is that in very narrow valleys the CBF is not necessarily stronger than in 0.5–1-km basins. Other effects, such as increased shadowing in smaller basins and valleys, need also to be taken into account, however.

Within the range of basin widths for which a CBF is possible, the actual occurrence of a CBF depends strongly on the stratification of the basin atmosphere, that is, whether it is stable and decoupled from the atmosphere aloft or neutral and coupled to the atmosphere aloft. Diurnal heating and destabilization of the basin atmosphere can thus lead to a regime change with respect to the occurrence of a CBF. A pure CBF with a return flow aloft occurs mainly under stable conditions; therefore, we call this area in Fig. 15 the *CBF regime*. The general circulation pattern in the CBF regime depends strongly on the direction of the background wind above the basin. The thermal forcing produces a closed circulation cell with a CBF toward the warmer sidewall near the basin floor and an RF in the opposite direction aloft. In a similar way, the background wind induces a circulation cell in the upper part of the basin, with a return flow opposing the background wind. The combination of the two vortices thus determines the circulation pattern inside the basin:

1) If the background wind points in the same direction as the temperature gradient ($\Delta\alpha = 0°$), two counterrotating cells form, strengthening the thermal RF.
2) If the background wind points in the opposite direction from the temperature gradient ($\Delta\alpha = 180°$), one basin-sized cell forms; that is, the thermal RF makes a smooth transition into the background wind.
3) If the background wind is perpendicular to the temperature gradient ($\Delta\alpha = 90°$), again two cells form, but with perpendicular rotation axes, resulting in a combined RF in the direction between the background-wind direction and the direction of the temperature gradient.

These results agree also with the findings from simulations in street canyons. Sini et al. (1996) and Xie et al.

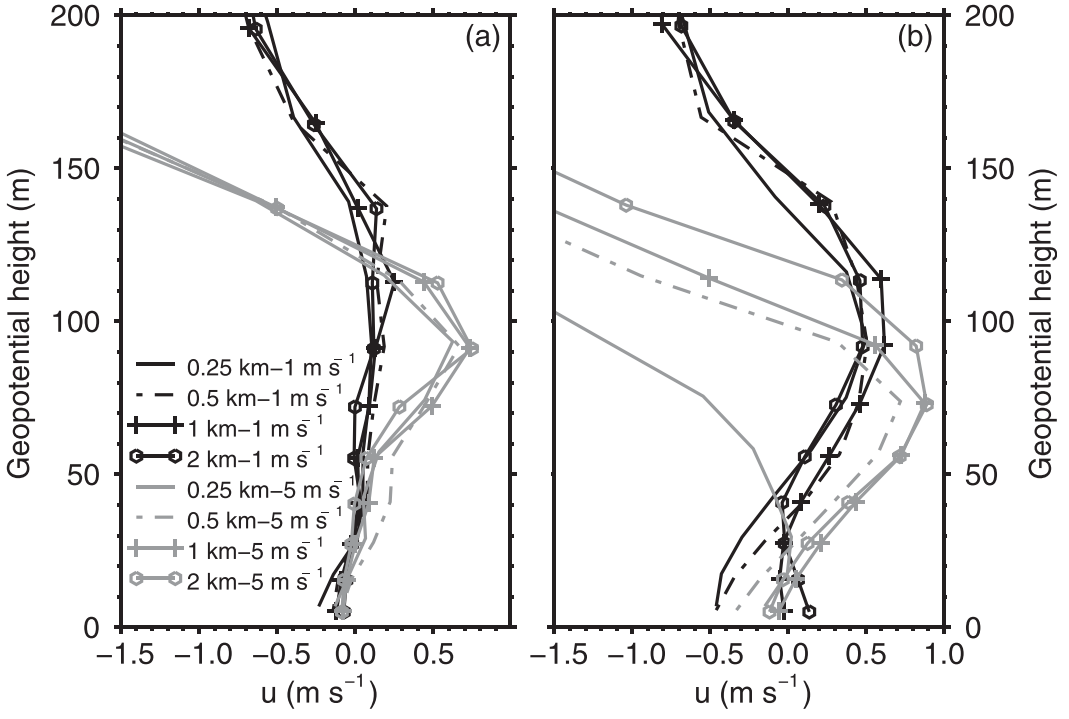

FIG. 14. Vertical profiles of the east–west wind component in the center of the basin at (a) +2.0 and (b) +3.0 h for different basin widths and 1 and 5 m s^{-1} easterly background winds.

(2005) found that for a flow perpendicular to the street canyon the resulting vortex in the canyon is enhanced if the leeward wall is heated and that two counterrotating vortices form if the windward wall is heated. The combination of a thermally induced and a background-wind-induced circulation in a street canyon is thus comparable to the circulation in larger mountain valleys or basins. The deeper topography of our model basins relative to a typical street canyon, however, seems to produce a strong spatial confinement of the background-wind-induced circulation cell to the top of the basin, particularly under stable conditions. The thermally driven circulation near the surface remains thus mostly sheltered from the background winds aloft so that the background-wind-induced circulation modifies the thermal circulation and not vice versa.

The current study is restricted to circular basin topographies. This means that the obstacle (i.e., the basin and its rim) is always aligned in the along-flow direction of the background wind, independent of the wind direction. The air is thus forced either above or around the obstacle. In a valley, however, background winds can be in the along-valley direction, leading to a channeling of the winds by the valley, which most likely leads to a different interaction with the thermal circulation. This restriction, however, is only relevant for the case $\Delta\alpha = 90°$ because of the orientation of the cross-valley circulation.

The direction of the CBF near the basin floor remains unaffected by the background wind under stable conditions. The strength of the background wind influences the strength and the depth of the CBF and the RF, however. It also influences the circulation pattern indirectly, as stronger background winds lead to slightly stronger mixing and an earlier coupling of the basin to the atmosphere aloft and, thus, to a transition to a different regime.

In the neutral basin atmosphere the background wind plays a more dominant role (*background-wind regime*). The background wind penetrates down into the basin, reaching the basin floor in the greater part of the basin. Near the upwind sidewall, however, a shallow thermal circulation is maintained along part of the floor and the sidewall. The size of the eddy that is formed by the thermal circulation in the lower upwind part of the basin depends on the local heat flux and the strength of the background wind. For strong background winds and a low local heat flux, the thermal circulation is very weak (small eddy) or is even nonexistent. It seems also likely that the basin depth has an impact on the penetration of the background wind and whether it reaches the basin floor. A systematic investigation of the influence of the basin depth on the cross-basin circulation was not, however, part of this study. Also, we did not investigate the effect of atmospheric stratification on the interaction

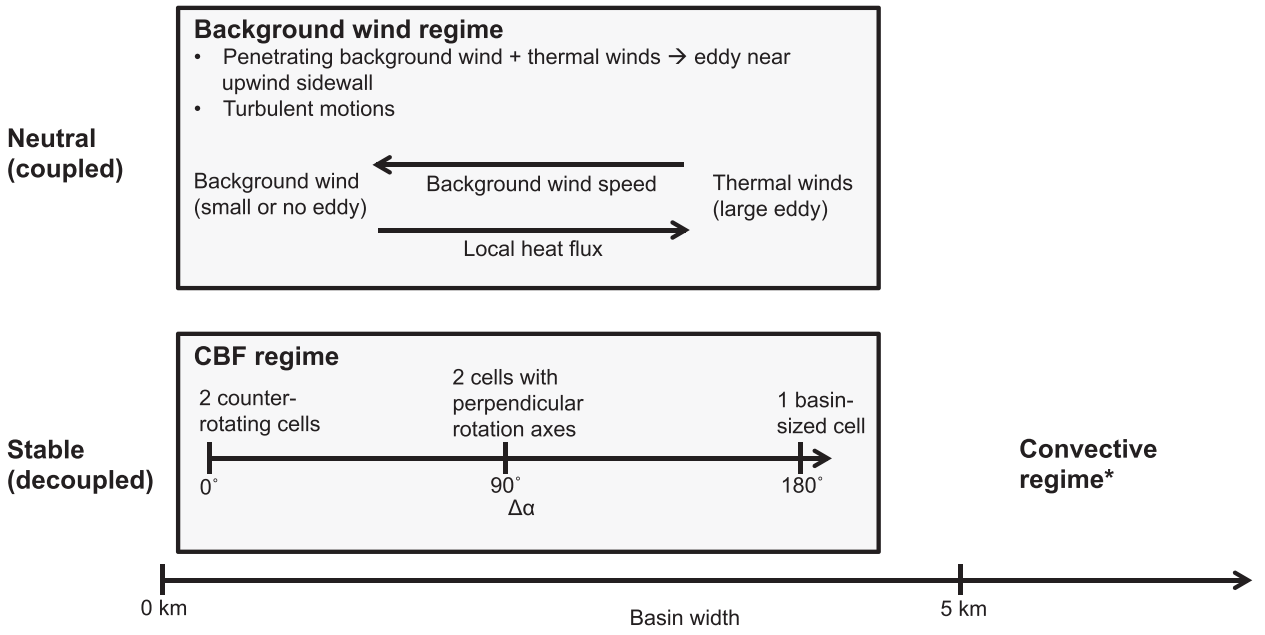

*) No simulations were run with background wind for the 5- and 10-km basins.

FIG. 15. Summary of the model results.

between the background wind and the thermally driven cross-basin circulation systematically. Inhomogeneities in the vertical temperature profile, such as elevated inversion layers, may induce additional cross-basin flows (e.g., Vergeiner and Dreiseitl 1987; Lehner and Gohm 2010) or may prevent the neutral basin atmosphere from coupling to the atmosphere aloft.

Lehner et al. (2011) found that thermal cross-basin winds in the Meteor Crater are disturbed if the background wind above the crater is too strong. They suggested that background winds form a basin-sized eddy when background winds exceeded a threshold of 4 m s^{-1}. They also tested 3 and 5 m s^{-1}, with little difference in the results. In our simulations, background winds produce a vortex under stable conditions, which, however, does not affect the surface CBF. Under neutral conditions, on the other hand, background winds strongly influence the surface CBF, but they are simply mixed down into the basin and do not form an eddy. The wind thresholds agree qualitatively with our simulations under neutral conditions for the 500-m basin, which is comparable in size to the Meteor Crater. For westerly background winds, the thermal circulation near the surface prevailed in the greater part of the basin for 1 m s^{-1} and, in the west half, for 2 m s^{-1} background winds, but background winds determined the surface wind field for higher wind speeds. We have to consider, however, that this result depends also on the direction of the background wind and the local heat flux (Fig. 15) and that CBF direction in the Meteor Crater varies continuously throughout the day.

Acknowledgments. We thank Sebastian Hoch (University of Utah) for helpful discussions. Author ML is a recipient of a DOC-fFORTE fellowship from the Austrian Academy of Sciences. This paper is based upon work supported by the National Science Foundation (NSF) under Grant AGS-0837870. Any opinion, findings, and conclusions or recommendations expressed in this material are those of the authors and do not necessarily reflect the views of the NSF. An allocation of computer time from the Center for High Performance Computing at the University of Utah is gratefully acknowledged. We also thank two anonymous reviewers for useful comments on the manuscript.

REFERENCES

Antonelli, M., and R. Rotunno, 2007: Large-eddy simulation of the onset of the sea breeze. *J. Atmos. Sci.,* **64,** 4445–4457.

Axelsen, S. L., and H. van Dop, 2009: Large-eddy simulation of katabatic winds. Part 1: Comparison with observations. *Acta Geophys.,* **57,** 803–836.

Catalano, F., and A. Cenedese, 2010: High-resolution numerical modeling of thermally driven slope winds in a valley with strong capping. *J. Appl. Meteor. Climatol.,* **49,** 1859–1880.

——, and C.-H. Moeng, 2010: Large-eddy simulation of the daytime boundary layer in an idealized valley using the Weather

Research and Forecasting numerical model. *Bound.-Layer Meteor.,* **137,** 49–75.

Chen, F., and J. Dudhia, 2001: Coupling an advanced land surface–hydrology model with the Penn State–NCAR MM5 modeling system. Part I: Model implementation and sensitivity. *Mon. Wea. Rev.,* **129,** 569–585.

Gleeson, T. A., 1951: On the theory of cross-valley winds arising from differential heating of the slopes. *J. Meteor.,* **8,** 398–405.

Hennemuth, B., 1986: Thermal asymmetries and cross-valley circulation in a small Alpine valley. *Bound.-Layer Meteor.,* **36,** 371–394.

——, and H. Schmidt, 1985: Wind phenomena in the Dischma Valley during DISKUS. *Arch. Meteor. Geophys. Bioklimatol.,* **B35,** 361–387.

Hoch, S. W., and C. D. Whiteman, 2010: Topographic effects on the surface radiation balance in and around Arizona's Meteor Crater. *J. Appl. Meteor. Climatol.,* **49,** 1114–1128.

Janjić, Z. I., 1994: The step-mountain eta coordinate model: Further developments of the convection, viscous sublayer, and turbulence closure schemes. *Mon. Wea. Rev.,* **122,** 927–945.

Knievel, J. C., G. H. Bryan, and J. P. Hacker, 2007: Explicit numerical diffusion in the WRF model. *Mon. Wea. Rev.,* **135,** 3808–3824.

Kuwagata, T., and F. Kimura, 1997: Daytime boundary layer evolution in a deep valley. Part II: Numerical simulation of the cross-valley circulation. *J. Appl. Meteor.,* **36,** 883–895.

Lehner, M., and A. Gohm, 2010: Idealised simulations of daytime pollution transport in a steep valley and its sensitivity to thermal stratification and surface albedo. *Bound.-Layer Meteor.,* **134,** 327–351.

——, C. D. Whiteman, and S. W. Hoch, 2011: Diurnal cycle of thermally driven cross-basin winds in Arizona's Meteor Crater. *J. Appl. Meteor. Climatol.,* **50,** 729–744.

MacHattie, L. B., 1968: Kananaskis Valley winds in summer. *J. Appl. Meteor.,* **7,** 348–352.

Matzinger, N., M. Andretta, E. van Gorsel, R. Vogt, A. Ohmura, and M. W. Rotach, 2003: Surface radiation budget in an Alpine valley. *Quart. J. Roy. Meteor. Soc.,* **129,** 877–895.

Mirocha, J. D., J. K. Lundquist, and B. Kosović, 2010: Implementation of a nonlinear subfilter turbulence stress model for large-eddy simulation in the Advanced Research WRF model. *Mon. Wea. Rev.,* **138,** 4212–4228.

Moeng, C.-H., J. Dudhia, J. Klemp, and P. Sullivan, 2007: Examining two-way grid nesting for large eddy simulation of the PBL using the WRF model. *Mon. Wea. Rev.,* **135,** 2295–2311.

Nakamura, Y., and T. R. Oke, 1988: Wind, temperature and stability conditions in an east-west oriented urban canyon. *Atmos. Environ.,* **22,** 2691–2700.

Niachou, K., I. Livada, and M. Santamouris, 2008: Experimental study of temperature and airflow distribution inside an urban street canyon during hot summer weather conditions. Part II: Airflow analysis. *Build. Environ.,* **43,** 1393–1403.

Offerle, B., I. Eliasson, C. S. B. Grimmond, and B. Holmer, 2007: Surface heating in relation to air temperature, wind and turbulence in an urban street canyon. *Bound.-Layer Meteor.,* **122,** 273–292.

Rampanelli, G., D. Zardi, and R. Rotunno, 2004: Mechanisms of up-valley winds. *J. Atmos. Sci.,* **61,** 3097–3111.

Scotti, A., C. Meneveau, and D. K. Lilly, 1993: Generalized Smagorinsky model for anisotropic grids. *Phys. Fluids,* **A5,** 2306–2308.

Sini, J.-F., S. Anquetin, and P. G. Mestayer, 1996: Pollutant dispersion and thermal effects in urban street canyons. *Atmos. Environ.,* **30,** 2659–2677.

Skamarock, W. C., and Coauthors, 2008: A description of the Advanced Research WRF version 3. NCAR Tech. Note NCAR/TN-475+STR, 113 pp.

Smith, C. M., and E. D. Skyllingstad, 2005: Numerical simulation of katabatic flow with changing slope angle. *Mon. Wea. Rev.,* **133,** 3065–3080.

Urfer-Henneberger, C., 1970: Neuere Beobachtungen über die Entwicklung des Schönwetterwindsystems in einem V-förmigen Alpental (Dischmatal bei Davos) [New observations of the development of fair-weather wind systems in a V-shaped Alpine valley (Dischmatal near Davos)]. *Arch. Meteor. Geophys. Bioklimatol.,* **B18,** 21–42.

Vergeiner, I., and E. Dreiseitl, 1987: Valley winds and slope winds—Observations and elementary thoughts. *Meteor. Atmos. Phys.,* **36,** 264–286.

Whiteman, C. D., K. J. Allwine, L. J. Fritschen, M. M. Orgill, and J. R. Simpson, 1989: Deep valley radiation and surface energy budget microclimates. Part II: Energy budget. *J. Appl. Meteor.,* **28,** 427–437.

——, and Coauthors, 2008: METCRAX 2006—Meteorological experiments in Arizona's Meteor Crater. *Bull. Amer. Meteor. Soc.,* **89,** 1665–1680.

Xie, X., Z. Huang, J. Wang, and Z. Xie, 2005: The impact of solar radiation and street layout on pollutant dispersion in street canyon. *Build. Environ.,* **40,** 201–212.